

# Strain Field Characteristics of Coal-like Material under CO<sub>2</sub> Fracturing

Published as part of the ACS Omega virtual special issue "CO<sub>2</sub> Geostorage".

Kang Wang,\* Hongyu Pan,\* and Yoshiaki Fujii



Cite This: *ACS Omega* 2023, 8, 33712–33722

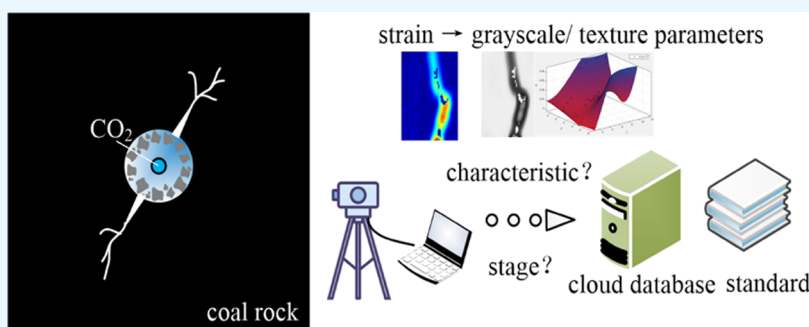


Read Online

ACCESS |

Metrics & More

Article Recommendations



**ABSTRACT:** Considering the problems related to hydrofracturing, CO<sub>2</sub> fracturing is a more effective way to enhance the permeability of coal seams. Conventional research has focused on the dynamic behavior of coal and rock under CO<sub>2</sub> fracturing. There is a lack of quantitative descriptions of the fracturing stages. Therefore, CO<sub>2</sub> fracturing experiments were carried out with coal-like material at several pressures. The maximum principal strain field was obtained by analyzing the surface images of the specimens. Nine characteristic parameters of typical grayscale and texture images were calculated from the strain field. The correlation between the maximum principal strain and the characteristic parameters was examined using gray relational analysis, and the effects of pressure on those parameters were investigated. We obtained some interesting results, for example, the standard deviation increased from 50 to 100, and kurtosis decreased from  $-1.0$  to  $-1.5$  with the fracturing pressure. The thresholds of the characteristic function  $F$  at different fracturing stages were determined, too. This research provides a basis for designing the drilling hole location and determining the millisecond delay of multihole fracturing, as well as for automatically dividing the fracturing stages with artificial intelligence based on the maximum principal strain field.

## 1. INTRODUCTION

Chinese carbon emissions are the highest worldwide. The Chinese government has made many attempts, including carbon capture, utilization, and storage (CCUS), to reduce CO<sub>2</sub> emissions. One CCUS technology, CO<sub>2</sub>-enhanced coalbed methane (CO<sub>2</sub>-ECBM) recovery, has received widespread attention.<sup>1</sup> However, hydraulic fracturing, which is used for ECBM recovery, has problems such as the water lock effect of coal and rock strata,<sup>2</sup> considerable water usage,<sup>3,4</sup> and difficulty of CH<sub>4</sub> flow.<sup>5</sup> Although base fluids and proppants can enhance the effect of conventional hydraulic fracturing, their damage to the formation and the high cost are still challenges.<sup>6</sup> Considering the above shortcomings, new fracturing methods such as pulse fracturing,<sup>7</sup> circulating thermochemical fluid fracturing,<sup>8</sup> and CO<sub>2</sub> fracturing have been proposed, and they have achieved good effects in recent years. Among them, CO<sub>2</sub> fracturing is a much better and more effective way to enhance the permeability of coal seams, as there have been various CO<sub>2</sub>

fracturing applications in low-permeability coal seams.<sup>9–11</sup> Research on the fracturing and propagation mechanism of coal during CO<sub>2</sub> fracturing plays a vital role in improving the recovery of coalbed methane and the CO<sub>2</sub> injection rate. This technique can also reduce gas disasters by degassing.<sup>12</sup>

Researchers have conducted many studies on the fracture propagation mechanism, fracture sizes, and morphological characteristics of fracture networks in coal and rock under the action of CO<sub>2</sub> fracturing.<sup>13–17</sup> Yu studied the influence of gas pressure and reservoir heterogeneity on coal seam permeability enhancement by CO<sub>2</sub> fracturing.<sup>18</sup> Yan investigated the

**Received:** June 8, 2023

**Accepted:** August 18, 2023

**Published:** September 5, 2023



fracture distribution in coal and rock under multifield coupling conditions such as CO<sub>2</sub> injection, crustal stress, and temperature.<sup>19</sup> Yang presented the results of field tests suggesting that an increase in fracturing pressure produces complex fracture structures.<sup>20</sup> Currently, research on the mechanism of CO<sub>2</sub> fracturing focuses on the experimental characterization of fractures. However, with the rapid development of monitoring methods, researchers have tried more quantitative analyses.

Multiple monitoring methods can better quantitatively study the failure mechanism of rocks and mutually verify the accuracy of their results. The commonly used monitoring parameters include acoustic emissions, pore distribution, strain, etc. They are necessary to study the failure and propagation mechanism during CO<sub>2</sub> fracturing.<sup>21</sup> Wang conducted CO<sub>2</sub> fracturing of coal briquettes and quantitatively analyzed the acceleration signals to obtain the time variation of the characteristic parameters.<sup>22</sup> Sampath used computed tomography (CT) scanning and scanning electron microscopy (SEM) to analyze the mechanism of supercritical CO<sub>2</sub> fracturing of heterogeneous coal specimens. The change in coal microstructure was obtained through image calculations.<sup>23</sup> Xing studied the evolution of the strain field of CO<sub>2</sub>-saturated sandstone under compression at a high strain rate.<sup>24</sup> Shang studied the dynamic process of liquid CO<sub>2</sub> fracturing by analyzing surface strain data.<sup>25</sup> Cai concluded through strain monitoring that smaller strain could be obtained when fracturing vent holes are distributed in the direction perpendicular to the rock bedding plane.<sup>26</sup> Wang performed CO<sub>2</sub> fracturing for preexisting fractures and evaluated the energy field based on the principal strain field until failure.<sup>27</sup> Previous studies have shown that the evolution of rock strain localization bands objectively reflects coal and rock fracture propagation.<sup>28</sup> However, quantitative detection of the CO<sub>2</sub> fracturing stages is still lacking. Therefore, it is necessary to combine specific indicators with physical significance that can quantitatively reflect the dynamic change in the strain field to accurately quantify the fracturing stage.

Grayscale and texture parameters are vital to quantitatively describe image features and are widely applied in many fields, such as medicine, agriculture, and mining.<sup>29,30</sup> The strain field can reflect the dynamic, unstable process of coal failure,<sup>31</sup> and grayscale and texture features can accurately describe the fracturing stages of coal and rock, as previous studies have shown. Xu studied the crack initiation and propagation process in granite using the texture feature parameters of images and verified its feasibility in reflecting the rock failure mechanism.<sup>32</sup> Sun established a damage model based on texture features and studied the generation and propagation process of microcracks in coal under uniaxial compression.<sup>33</sup> By quantifying the strain field, Zhang studied the evolution of the grayscale and texture parameters in the strain field during the compressive deformation of fractured sandstone specimens.<sup>34</sup>

Given the insufficient quantitative research on the CO<sub>2</sub> fracturing-induced strain field and the unclear division of fracturing stages, we propose a new method based on image feature analysis. CO<sub>2</sub> fracturing of coal-like material at different pressures is carried out in this study to quantitatively analyze the grayscale and texture characteristic parameters of the strain field during fracturing. The fracturing stages are determined, and the features of the parameters are discussed. Threshold values of the characteristic parameters for each stage are presented. These results will be helpful for the automatic detection of fracturing stages based on image analysis and

artificial intelligence (AI) in the future. This work also provides a basis for designing drilling hole locations and determining millisecond delays for multihole fracturing.

## 2. MATERIALS AND METHODOLOGY

**2.1. Experimental System.** An original CO<sub>2</sub> fracturing testing platform was designed and manufactured, and a noncontact system was used to measure the strain field. The CO<sub>2</sub> fracturing test platform was mainly composed of loading, fracturing, and observation systems. The loading system was a DNS 200 electronic universal testing machine. Before the test, the basic physical and mechanical parameters of the specimen were obtained; the specimens were first loaded with a constant axial pressure. The CO<sub>2</sub> fracturing test system was composed of a CO<sub>2</sub> cylinder, pressure-reducing valve, high-pressure solenoid valve, pressure gauge, and explosion-proof inflation device; this device was convenient for releasing a constant pressure to fracture the coal-like material at the moment of fracturing. The testing system is shown in Figure 1.

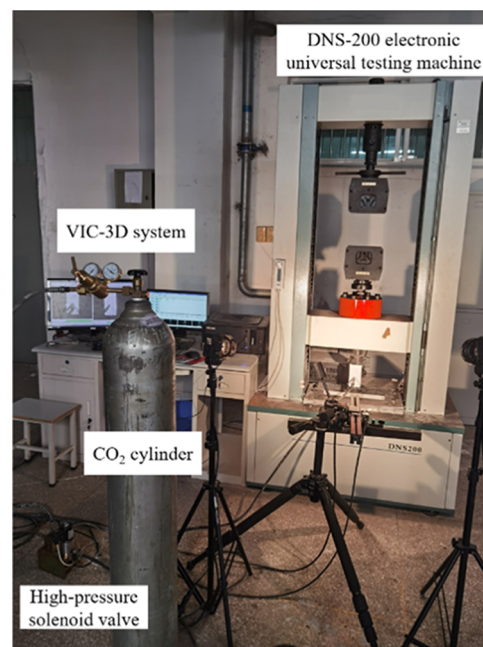


Figure 1. Experimental system.

**2.2. Specimens.** Coal is a heterogeneous and brittle material, often resulting in poor reproducibility of experiments.<sup>35</sup> In contrast, materials like polymethyl methacrylate (PMMA), which are typically homogeneous, exhibit markedly different mechanical properties compared to coal. To address this, recent studies have turned to coal-like materials.

That reflects the mechanical properties of coal. While being less heterogeneous, such materials include sand, lime, and gypsum (Wang G);<sup>36</sup> crushed coal, cement, and activated carbon (Wang G);<sup>37</sup> sand and paraffin (Wang X);<sup>38</sup> and cement, sand, coal powder, and gypsum (Zhai).<sup>39</sup> Moreover, to ensure the integrity of the specimen's fracturing tube, it is integrated during the molding process of the material as a single structure. This integration mitigates potential impacts on the material's strength and prevents gas leakage from the fracturing tubes.

Hence, we formulated coal-like specimens (Figure 2) to closely match the mechanical characteristics of coal. This was

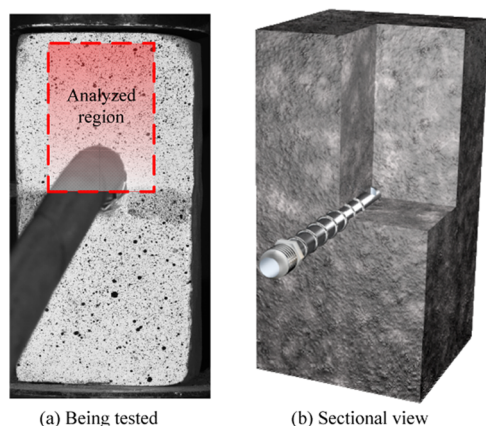


Figure 2. Coal-like specimen with the fracturing tube.

achieved by blending pulverized coal, cement, and gypsum.<sup>40</sup> Following numerous preliminary tests, the mass ratio of pulverized coal, cement, gypsum powder, and water was established at 1:2:1:1.2. The mechanical and physical properties were evaluated through various methods, including uniaxial compression tests and the ultrasonic pulse method. These outcomes are presented in Table 1.

The mixture was poured into a 70 mm × 70 mm × 140 mm rectangular mold. A 10 mm  $\phi$  fracturing tube was placed at the center of the mold after vibration to remove air. There were two 2 mm  $\phi$  vent holes at the end of the tube. The specimens were removed from the mold 72 h later. Then, they were kept at a temperature of 19–24 °C and relative humidity of 20–30%. After 28 days of curing, the specimen surfaces were polished and repaired if needed.

**2.3. Experimental Procedure.** Vaseline was applied on the upper and lower ends of the specimen to reduce friction. The loading rate was set at 0.05 kN/s, and when the prestress reached 4.9 kN (1.0 MPa), the load was kept through CO<sub>2</sub> fracturing.

Previous studies<sup>41,42</sup> have shown that an increase in fluid pressure will lead to turbulence and other phenomena when flowing through the pore structure of coal and rock masses, which will have a certain impact on the fracturing effect. For these reasons, we chose to adopt CO<sub>2</sub> pressure. The specimens were fractured at a pressure of 1.0, 1.5, or 2.0 MPa, respectively.

A PMMA protecting plate established safety from large fragments. The VIC-Snap system collected the image of the region shown in Figure 2 during the fracturing process. The sampling interval was set at 1.0 ms to obtain the dynamic behavior of the strain field. Each group of experiments was repeated at least five times, and typical results were selected for analysis.

**2.4. Image Analysis Methodology.** The workflow diagram of the analysis methodology is shown in Figure 3.

(1) Grayscale feature parameters

Table 1. Physical and Mechanical Parameters<sup>a</sup>

$\rho$ /(kg·m <sup>-3</sup> )	$C_p$ /(m/s)	$C_s$ /(m/s)	$\sigma$ /MPa	$E$ /GPa	$\nu$	$C$ /MPa	$\phi$ /(deg)
$1.25 \times 10^3$	1860	1088	4.59	2.50	0.24	1.21	24.2

<sup>a</sup> $\rho$ : density,  $C_p$ : P-wave velocity,  $C_s$ : S-wave velocity,  $\sigma$ : uniaxial compressive strength,  $E$ : Young's modulus,  $\nu$ : Poisson's ratio,  $C$ : cohesion, and  $\phi$ : internal friction angle.

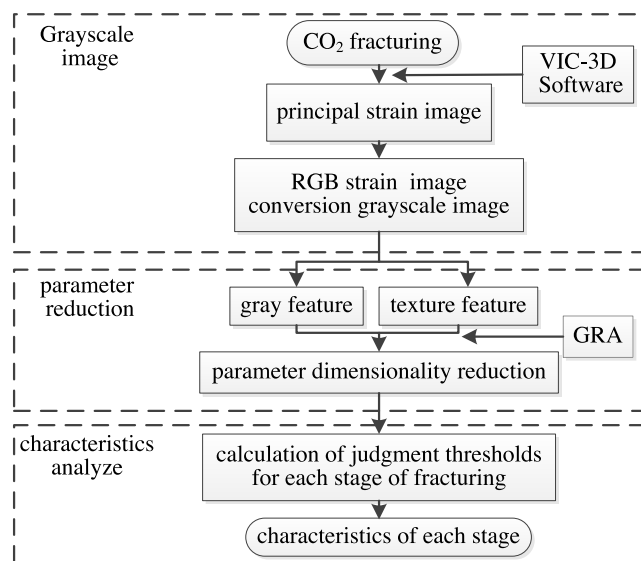


Figure 3. Workflow diagram.

The VIC-3D software calculates the maximum principal strain field from the specimen surface image taken by the VIC-Snap system. The maximum principal strain of 0 to 0.0707 was converted from blue to red on a color scale. Then, the color scale was converted to 0–255 grayscale  $i$  by eq 1.<sup>43</sup>

$$i = 0.299R + 0.587G + 0.114B \quad (1)$$

The mean, standard deviation, skewness, kurtosis, and energy parameters were evaluated. The above parameters<sup>44</sup> are defined in Table 2, where  $p(i)$  is the probability of the  $i$ th

Table 2. Grayscale Characteristic Parameters

symbol	name	definition	statistical meaning
$g_1$	mean	$m = \sum_{i=0}^{255} p(i)$	the average value of grayscale
$g_2$	standard deviation	$\sigma = \sqrt{\sum_{i=0}^{255} (i - m)^2 p(i)}$	dispersion of grayscale
$g_3$	skewness	$S = \frac{1}{\sigma^3} \sum_{i=0}^{255} (i - m)^3 p(i)$	asymmetric degree of gray distribution
$g_4$	kurtosis	$K = \frac{1}{\sigma^4} \sum_{i=0}^{255} (i - m)^4 p(i) - 3$	the degree to which the gray distribution is concentrated near the mean value
$g_5$	energy	$E = \sum_{i=0}^{255} p(i)^2$	uniformity of gray distribution

gray level,<sup>45</sup>  $n_i$  is the number of pixels with the  $i$ th gray level, and  $N$  is the total number of pixels.

$$p(i) = \frac{n_i}{N} \quad (2)$$

(2) Texture feature parameters

The gray level cooccurrence matrix (GLCM) method proposed by Haralick<sup>46</sup> was used to evaluate spatial correlation features.  $F(x,y)$  was set for the two-dimensional digital image

Table 3. Texture Feature Parameters

symbol	name	definition	statistical meaning
$f_1$	contrast	$f_1 = \sum_{i,j} (i - j)^2 P(i, j)$	the gray level difference between adjacent pixels
$f_2$	correlation	$f_2 = \frac{1}{\sigma_i \sigma_j} \sum_{i,j} (i - \mu_i)(j - \mu_j) P(i, j)$	the gray level similarity between adjacent pixels
$f_3$	ASM	$f_3 = \sum_{i,j} P^2(i, j)$	evenness of pixel gray level distribution
$f_4$	homogeneity	$f_4 = \sum_{i,j} \frac{P(i, j)}{1 +  i - j }$	the complexity of pixel grayscale

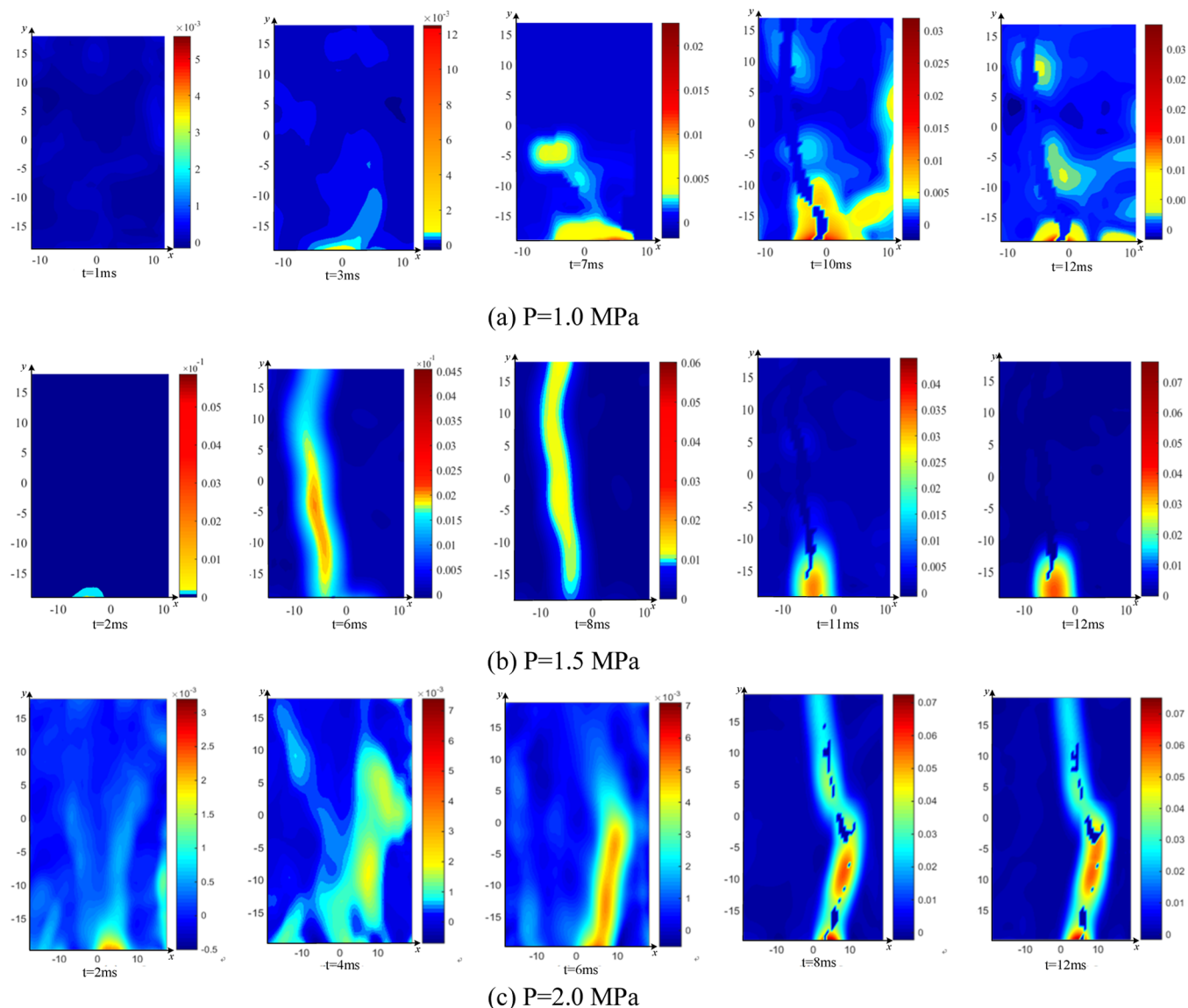


Figure 4. Maximum principal strain distribution.

with size  $M \times N$  pixels whose gray level is  $N_g$ . Then, starting from the pixel with gray level  $i$  and position  $(x_1, y_1)$  to the pixel with gray level  $j$  and distance  $d$  and position  $(x_2, y_2)$ , the frequency of simultaneous occurrence  $P(i, j) = \{(x_1, y_1), (x_2, y_2) \in M \times N | f(x_1, y_1) = i, f(x_2, y_2) = j\}$  was calculated. Contrast, correlation, angular second moment (ASM), and homogeneity were evaluated as the four parameters of gray-level cooccurrence (Table 3).

- (3) Characteristic equation of the strain field based on gray relational analysis (GRA)

Correlation analysis by GRA was carried out to explore the correlation between characteristic parameters and maximum principal strain, to determine the importance and to eliminate redundant factors with low correlation in the characteristic space  $\Omega = \{x_1, x_2, \dots, x_9\}$ .<sup>47</sup> GRA is a measure of the degree of correlation between factors of known systems that change with time, which reflects the degree of similarity or difference in the development trend between factors.<sup>48</sup> The maximum principal strain is selected as the reference sequence, and the parameters are the comparison sequence. The resolution coefficient  $\rho$  is 0.5. The average value of specimen data  $X$  and the standard

deviation of the specimen were set as  $\mu$  and  $S$  to remove the dimension influence. The data are standardized, that is,  $x_i = (x_i - \mu)/S$ . Equation 3<sup>49</sup> calculates the gray correlation coefficient  $\xi$ .

$$\xi_{0i} = \frac{\Delta(\min) + \rho\Delta(\max)}{\Delta_{0i}(k) + \rho\Delta(\max)} \quad (3)$$

where  $\Delta(\min)$  and  $\Delta(\max)$  are the maximum and minimum values of the range difference between the comparison and reference columns, respectively.

Then, the correlation degree  $r$  of all data  $X_N$  can be expressed as

$$r_i = \frac{1}{N} \sum_{k=1}^N \xi_i(k) \quad (4)$$

The characteristic equation can be expressed as

$$F = \sum_1^5 r_m g_m + \sum_1^4 r_n f_n \quad (5)$$

where  $r_m$  and  $r_n$  are the correlation coefficients after removing the low correlation degree, and  $g_m$  and  $f_n$  are the feature parameters after removing the low correlation.

### 3. RESULTS

**3.1. Maximum Principal Strain.** For the 1.0 MPa CO<sub>2</sub> pressure case, the fracturing process lasted 12 ms in total (Figure 4a). The fracturing stages can be divided into three stages. In the first stage, 0–3 ms, the maximum principal strain was uniformly distributed even around the vent holes. In the second stage, 3–7 ms, a banded stress localization zone appeared, and the strain concentration in the middle of the specimen may indicate a weaker portion. The specimen was split in the third stage, 7–12 ms. At this time, the existing damage and fractures would have induced the formation of secondary fractures.<sup>50</sup> The maximum principal strain was still concentrated around the vent holes. The uneven color patches in the strain localization band were caused by spalling of the specimen's surface.

For the 1.5 MPa case (Figure 4b), the increased pressure shortens the time of the first stage. The deformation localization gradually became more apparent in the second 2–6 ms stage. The specimen was split in the third stage, 6–12 ms, and the strain concentration was apparent around the bent holes.

For the 2.0 MPa case (Figure 4c), in the second stage,  $2 \leq t \leq 6$  ms, the initial damage and deformation localization band were formed far from the hole under the synergetic action of the stress wave and CO<sub>2</sub> high pressure. In the third stage,  $6 \leq t \leq 12$  ms, the specimen was split. A fracture appeared in the localization zone.

The maximum principal strain values at each stage are summarized in Table 4.

Traditional fracturing stage division methods, including the above division, often rely on strain data to visually evaluate sudden jump values or numerical trends, lacking objectiveness and quantitiveness. Therefore, image analyses should be carried out.

**3.2. Correlation of Characteristic Parameters.** The Kaiser–Meyer–Olkin (KMO) value of the standardized data was 0.76, and the corresponding  $P$  value of the Bartlett test was far less than 0.05, indicating that it was suitable for correlation

**Table 4. Highest Maximum Principal Strain Values for Each Stage**

pressure	stage	time (ms)	maximum principal strain
1.0 MPa	I	0–3	0.0005
	II	3–7	0.0141
	III	7–12	0.0142
1.5 MPa	I	0–2	0.0008
	II	2–6	0.0138
	III	6–12	0.0155
2.0 MPa	I	0–2	0.0049
	II	2–6	0.0197
	III	6–12	0.0430

analysis. The maximum principal strain was taken as the reference sequence, the corresponding characteristic parameters were the comparison sequence, and the resolution coefficient was taken as 0.5. The calculated characteristic parameters were ranked as shown in Table 5.

**Table 5. Parameter Correlation**

symbol	name	$r$	order
$f_2$	correlation	0.9907	1
$f_4$	homogeneity	0.9902	2
$g_1$	mean	0.9891	3
$f_1$	contrast	0.9726	4
$g_2$	standard deviation	0.9643	5
$f_3$	skewness	0.9575	6
$g_4$	kurtosis	0.9452	7
$g_3$	ASM	0.8592	8
$g_5$	energy	0.5767	9

According to Table 5, the correlation between the correlation and maximum principal strain was the largest, 0.991, which was the most crucial characteristic parameter of the strain distribution behavior. The correlation of the first seven parameters' values exceeded 0.9 and could be selected as the main parameters. However, the correlation between the maximum principal strain and ASM or energy was low. They could be eliminated to improve the calculation speed and enhance the accuracy of the maximum principal strain assessment so that the reduced seven-dimensional feature space could be obtained.

The reduced seven-dimensional feature space was used as the discriminant parameter for the critical period of the fracturing stage. The strain distribution characteristic value  $F$  was evaluated by eq 5, and the threshold value of the  $F$  comprehensive criterion was found (Figure 5 and Table 6).

**3.3. Parameter Characteristic Analysis.** Previous studies have shown that the image texture parameters reflect the fracturing stages.<sup>51</sup> The grayscale histogram changed from uniform "short and fat" to centralized "thin and tall" (Figure 6a). The normalized frequency peak increased with the fracturing stages (Figure 6a). The increase was significant for the low fracturing pressure, which may indicate that the higher pressure led to a thicker strain localization band so that the grayscale distribution became blunt. All parameters were affected by the fracturing pressure (Figure 6b).

Contrast and correlation were positively correlated with the fracturing stage, while ASM and homogeneity were negatively correlated. The characteristics of the parameters in each fracturing stage are as follows:

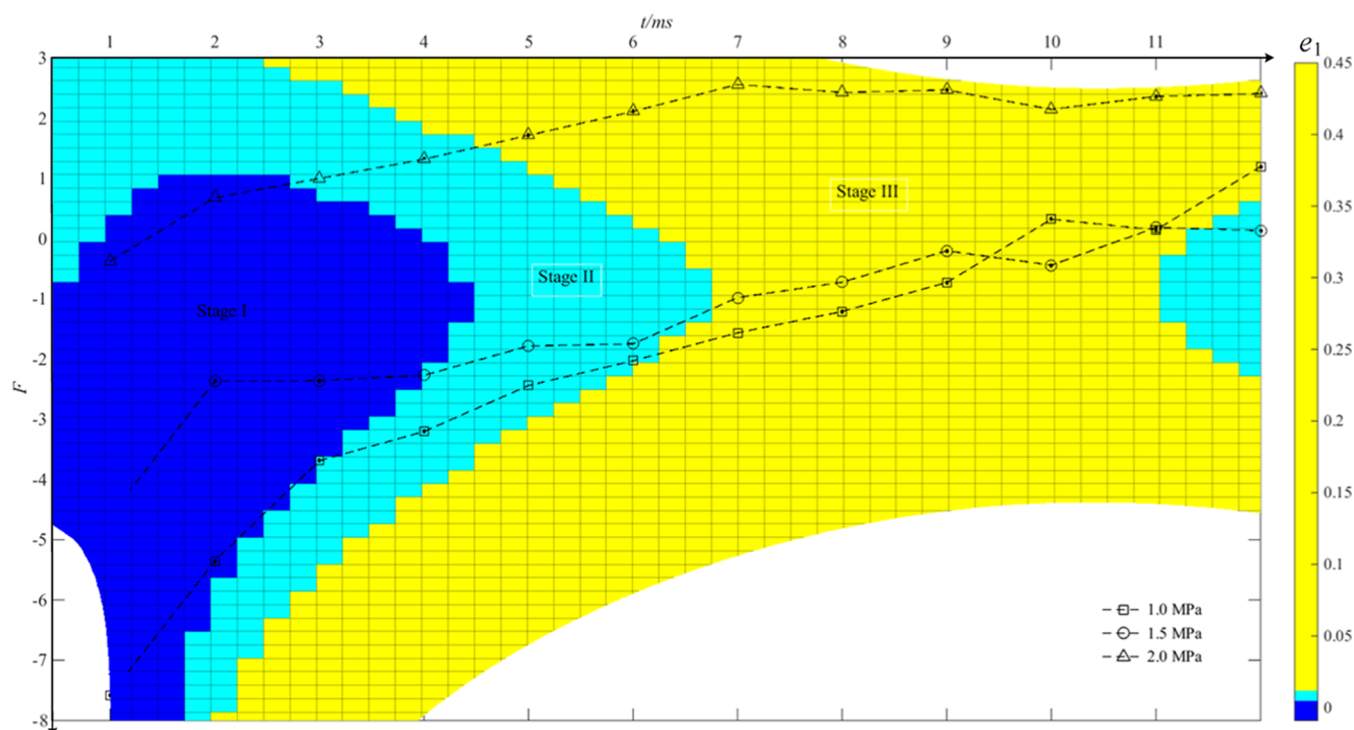


**Figure 5.** Time variation of  $F$  and fracturing stages. The fitting equation for the maximum principal strain  $e_1$  is  $e_1 = 0.007982 - 0.005158 t + 0.001262 F + 0.00149 t^2 + 0.0001733 tF - 0.0001973F^2 - 8.867 \times 10^{-5} t^3 + 1.887 \times 10^{-5} t^2F + 0.0002793 tF^2$ ;  $r^2 = 0.99$ ;  $t$  is in ms.

**Table 6.**  $F$  Thresholds

pressure	stage	time (ms)	$F$
1.0 MPa	I	3.0	-3.70
	II	7.0	-1.57
	III		
1.5 MPa	I	2.0	-2.40
	II	6.0	-1.75
	III		
2.0 MPa	I	2.0	0.68
	II	6.0	2.10
	III		

(1) Stage I:

The stress wave first impacted the specimen around the fracturing tube, resulting in strain concentration around the tube as the initial damage. The normalized frequency peak was relatively small, but the value increased at the end of the stage.

(2) Stage II:

At the beginning of this stage, strain localization began to appear, although the strain concentration around the hole was still more significant. The strain distribution was relatively uniform at this time. In the middle of this stage, the strain localization became clearer. Then, the strain concentration could be seen at the end of this stage.

(3) Stage III:

The shape of the grayscale histogram changed from a uniform distribution to a centralized distribution of 100–150 gray values, indicating the formation of deformation localization bands. The shape of the grayscale histogram after fracture generation remained unchanged. Contrast increased at the end of this stage due to the extensive specimen damage, indicating clear and deep texture grooves in the strain field.

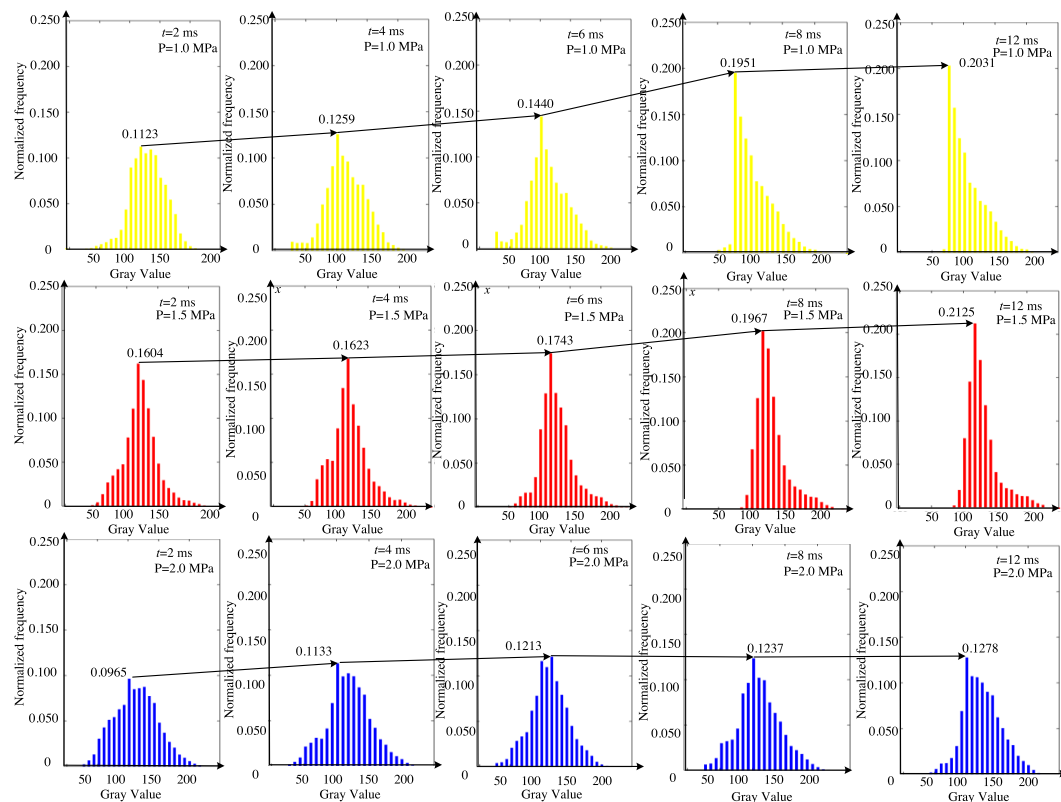
**3.4. Effects of Fracturing Pressure on the Characteristic Parameters.** Mean and kurtosis were negatively correlated with the initial fracturing pressure, while standard deviation, skewness, and energy were positively correlated with the initial fracturing pressure (Figure 7). The difference in grayscale parameters between 1.0 and 1.5 MPa was slight, while the grayscale parameters for 2.0 MPa differed from those for the other pressures.

The effect of pressure seems almost linear to contrast (Figure 8a), while the correlation increases only for 2.0 MPa (Figure 8b). High ASM and homogeneity values were observed for 1 MPa pressure (Figure 8c,d).

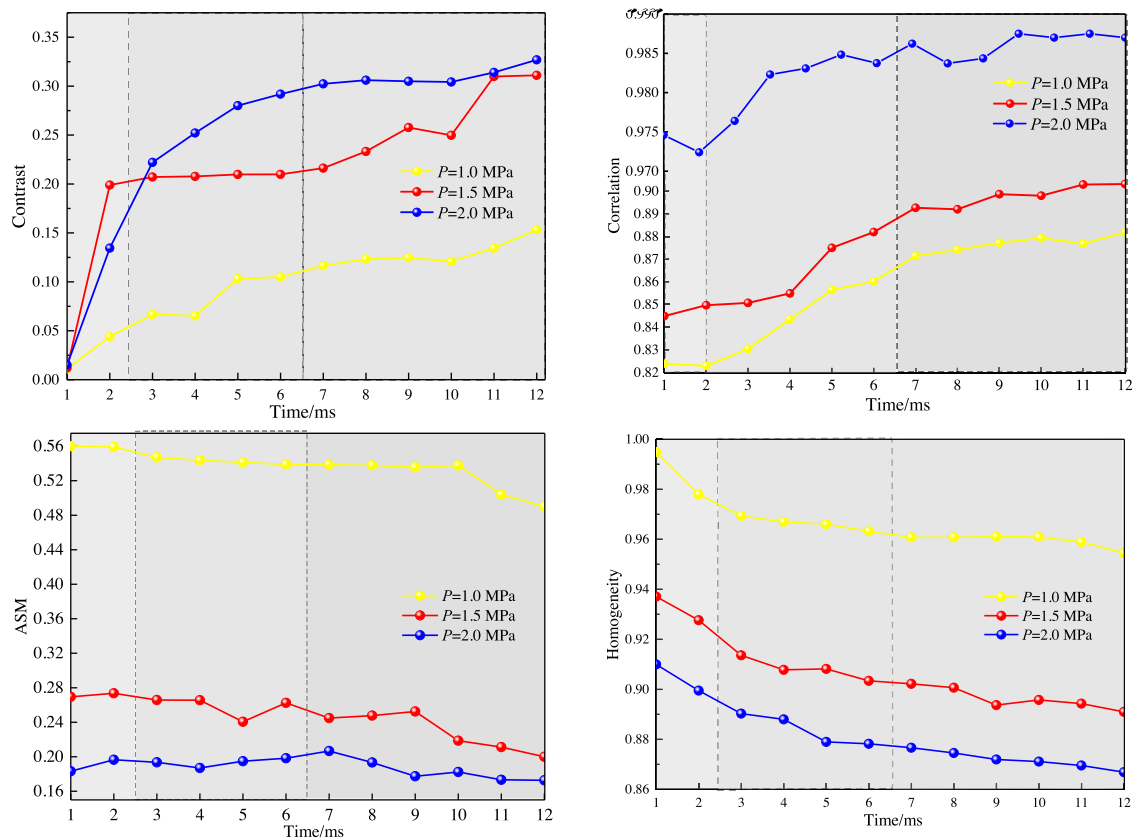
## 4. DISCUSSION

Predicting the fracture propagation and principal strain change in coal-like materials, not limited to coal alone, presents a challenging task. This endeavor often demands significant time and energy to ascertain the extent of fracture influence. Imaging analysis finds widespread utility in domains like medicine. For instance, we can deduce the pathological stage of lung cancer from X-ray images. Drawing inspiration from this, we propose harnessing image characteristics to infer the maximum principal strain field during the fracturing process and to determine stages of failure.

Looking ahead, AI image recognition technology holds promise for executing diverse tasks in intelligent coal mining



(a) Gray level histogram with the normalized frequency peak



(b) texture characteristic parameters

Figure 6. Graphics parametric curve.

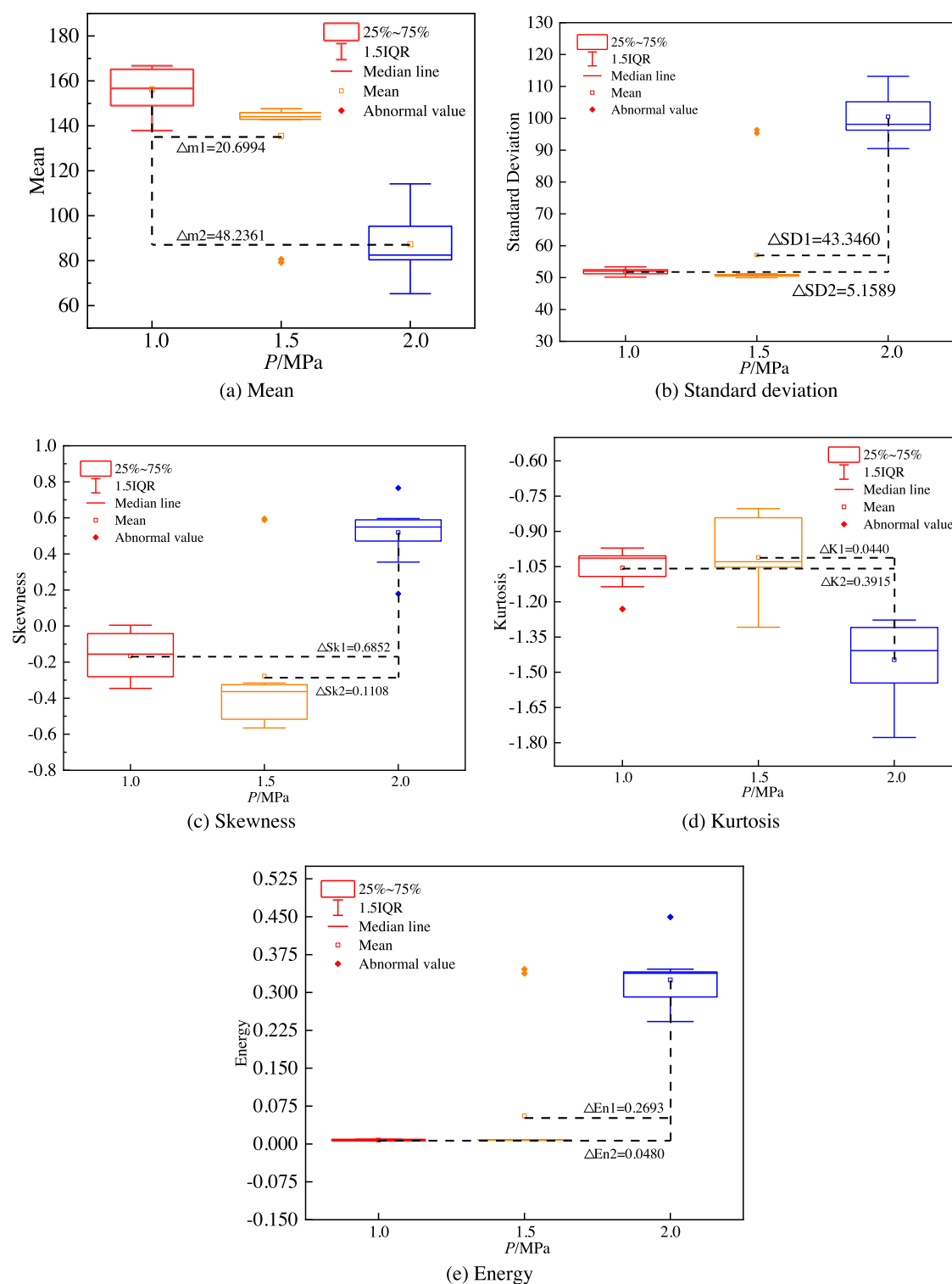


Figure 7. Characteristic parameters.

operations. A cloud-based database will be established, offering unfettered access to rock failure stage parameters for specific materials whenever required, contingent upon adequate data availability. Supported by ample testing and data, technical manuals and industrial standards will be formulated. Through these efforts, we aspire for this research to mark a significant stride toward progress.

A limitation of this study is that it solely employed uniaxial loading. The findings can be extrapolated to scenarios

involving the fracturing of shallowly buried coal and rock, as well as coal and rock containing numerous vertical faults, residual coal pillars, inclined coal seam slopes, and analogous rock-like materials without confining pressure. Nonetheless, for a more extensive range of applications, it becomes imperative to account for confining pressure within a closed-box environment, alongside the ramifications of CO<sub>2</sub> adsorption by coal, so we are conducting some new research to change these limitations.<sup>S2</sup>

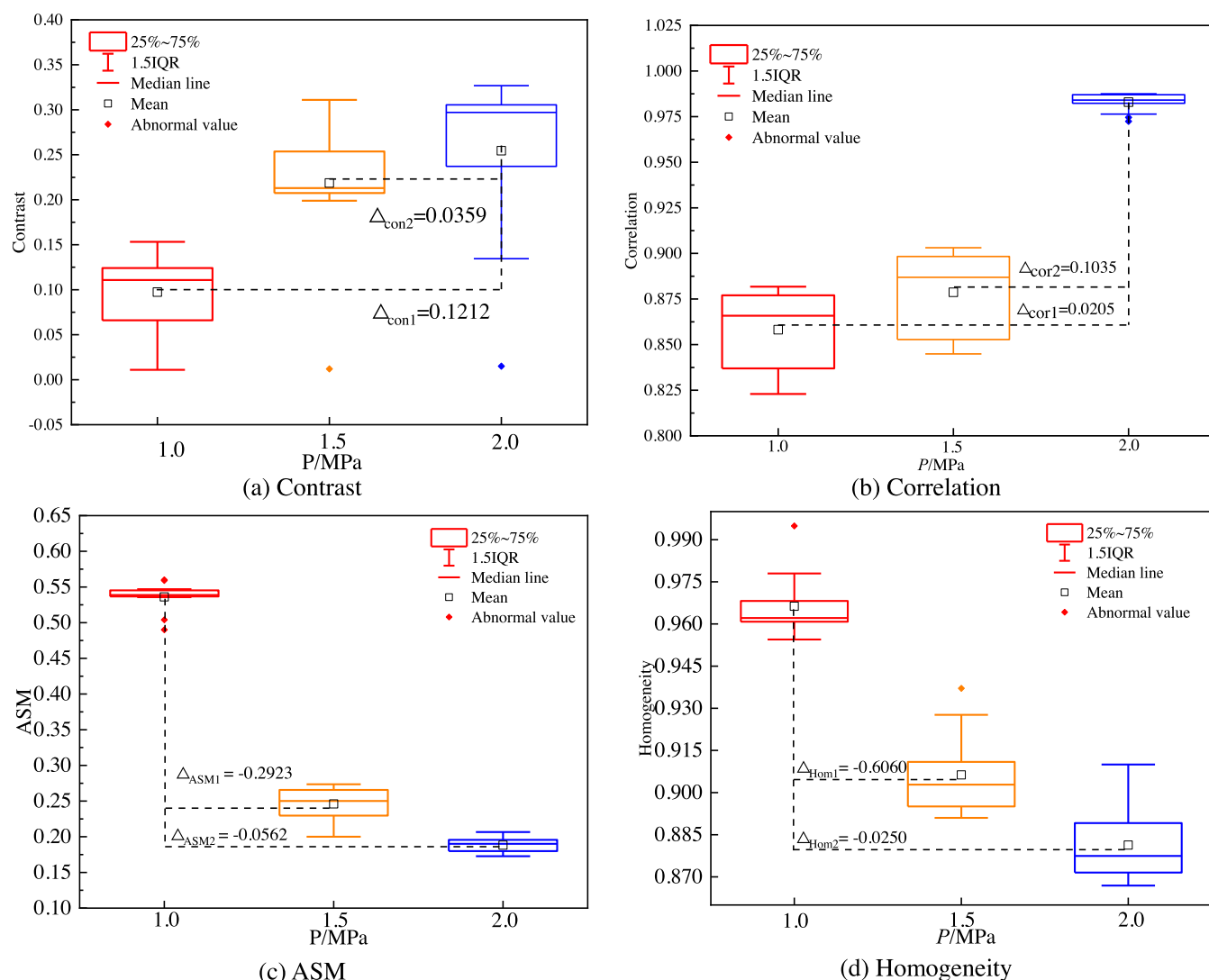


Figure 8. Texture parameters.

## 5. CONCLUSIONS

- (1) The grayscale parameters mean and kurtosis are negatively correlated with the initial pressure. Standard deviation, skewness, and energy are positively correlated with the initial fracturing pressure. The texture parameters contrast and correlation are positively correlated with time, and ASM and homogeneity are negatively correlated with time.
- (2) The characteristic parameter correlation order is correlation > homogeneity > mean > contrast > standard deviation > skewness > kurtosis. Among them, correlation and homogeneity are the largest, being 0.9907 and 0.9902, respectively.
- (3) There are three stages in the CO<sub>2</sub> fracturing of the strain field. (A) The stage of CO<sub>2</sub> fracturing stress wave action. The normalized frequency of the gray value is less than 0.1604, the texture parameters of the strain field all jump, and the grooved texture is obvious. (B) Stress wave-high pressure gas synergy stage. The strain field gradually forms a strain localization band from a uniform distribution, and the gray level distribution shifts to a lower gray level. (C) CO<sub>2</sub> splitting stage. The numerical change in the strain field is no longer obvious, the

generation of cracks in this band makes the grayscale histogram morphology transition from "short and fat" to "tall and thin", and the texture characteristic parameters fluctuate in a small range.

## AUTHOR INFORMATION

### Corresponding Authors

**Kang Wang** – College of Safety Science and Engineering, Xi'an University of Science and Technology, Xi'an 710054, China; Faculty of Engineering, Hokkaido University, Sapporo 060-8628, Japan; Email: [kliiek\\_618@163.com](mailto:kliiek_618@163.com)

**Hongyu Pan** – College of Safety Science and Engineering, Xi'an University of Science and Technology, Xi'an 710054, China; Email: [pan05016@126.com](mailto:pan05016@126.com)

### Author

**Yoshiaki Fujii** – Faculty of Engineering, Hokkaido University, Sapporo 060-8628, Japan

Complete contact information is available at:

<https://pubs.acs.org/10.1021/acsomega.3c04046>

### Notes

The authors declare no competing financial interest.

## ACKNOWLEDGMENTS

This research was financially supported by the National Natural Science Foundation of China (51874234, 52274226).

## NOMENCLATURE

GLCM, gray-level cooccurrence matrix; GRA, gray relational analysis; CCUS, carbon capture, utilization and storage; CO<sub>2</sub>-ECBM, CO<sub>2</sub>-enhanced coalbed methane; VIC-3D System, noncontact, full-field strain & deformation measurement system; KMO, Kaiser–Meyer–Olkin; F, threshold for judging the stage of CO<sub>2</sub> fracturing; AI, artificial intelligence

## REFERENCES

- (1) Jiang, K.; Ashworth, P.; Zhang, S.; et al. China's carbon capture, utilization and storage (CCUS) policy: A critical review. *Renewable Sustainable Energy Rev.* **2020**, *119*, No. 109601.
- (2) Wang, C.; Su, Y.; Wang, W.; et al. Water Blocking Damage Evaluation and Mitigation Method in Tight Gas Reservoirs. *Energy Fuels* **2022**, *36*, 10934–10944.
- (3) Middleton, R. S.; Carey, J. W.; Currier, R. P.; et al. Shale gas and non-aqueous fracturing fluids: Opportunities and challenges for supercritical CO<sub>2</sub>. *Appl. Energy* **2015**, *147*, 500–509.
- (4) Tariq, Z.; Mahmoud, M.; Abdurraheem, A.; et al. An environment friendly approach to reduce the breakdown pressure of high strength unconventional rocks by cyclic hydraulic fracturing. *J. Energy Resour. Technol.* **2020**, *142*, No. 043002.
- (5) Kalam, S.; Afagwu, C.; Al Jaber, J.; et al. A review on non-aqueous fracturing techniques in unconventional reservoirs. *J. Nat. Gas Sci. Eng.* **2021**, *95*, No. 104223.
- (6) Tariq, Z.; Mahmoud, M.; Abdurraheem, A. et al. In *A Review of Pulse Fracturing Treatment: an Emerging Stimulation Technique for Unconventional Reservoirs*, SPE Middle East Oil and Gas Show and Conference; 2019; p D041S041R001.
- (7) Tariq, Z.; Mahmoud, M.; Abdurraheem, A.; et al. An experimental study to reduce the breakdown pressure of the unconventional carbonate rock by cyclic injection of thermochemical fluids. *J. Pet. Sci. Eng.* **2020**, *187*, No. 106859.
- (8) Zhang, L.; Li, J.; Xue, J.; et al. Experimental studies on the changing characteristics of the gas flow capacity on bituminous coal in CO<sub>2</sub>-ECBM and N<sub>2</sub>-ECBM. *Fuel* **2021**, *291*, No. 120115.
- (9) Li, G. S.; Wang, H. Z.; Shen, Z. H.; et al. Application investigations and prospects of supercritical carbon dioxide jet in petroleum engineering. *J. China Univ. Pet.* **2013**, *37*, 76–87.
- (10) Mukherjee, M.; Misra, S. A review of experimental research on Enhanced Coal Bed Methane (ECBM) recovery via CO<sub>2</sub> sequestration. *Earth-Sci. Rev.* **2018**, *179*, 392–410.
- (11) Zhou, S.; Yao, Y.; Luo, X.; Jiang, N.; Niu, S. Dynamic Response Evaluation for Single-Hole Bench Carbon Dioxide Blasting Based on the Novel SSA–VMD–PCC Method. *Int. J. Geomech.* **2023**, *23*, No. 04022248.
- (12) Cai, C.; Kang, Y.; Wang, X.; et al. Mechanism of supercritical carbon dioxide (SC-CO<sub>2</sub>) hydro-jet fracturing. *J. CO<sub>2</sub> Util.* **2018**, *26*, 575–587.
- (13) Cong, Z.; Li, Y.; Pan, Y.; Liu, B.; Shi, Y.; Wei, J. Study on CO<sub>2</sub> foam fracturing model and fracture propagation simulation. *Energy* **2022**, *238*, No. 121778.
- (14) Yan, H.; Zhang, J.; Li, B.; Zhu, C. Crack propagation patterns and factors controlling complex crack network formation in coal bodies during tri-axial supercritical carbon dioxide fracturing. *Fuel* **2021**, *286*, No. 119381.
- (15) Zhang, Y.; Deng, J.; Deng, H.; Ke, B. Peridynamics simulation of rock fracturing under liquid carbon dioxide blasting. *Int. J. Damage Mech.* **2019**, *28*, 1038–1052.
- (16) Chen, H.; Hu, Y.; Kang, Y.; Wang, X.; Liu, F.; Liu, Y. Advantages of supercritical CO<sub>2</sub> compound fracturing in shale on fracture geometry, complexity and width. *J. Nat. Gas Sci. Eng.* **2021**, *93*, No. 104033.
- (17) Wang, L.; Yao, B.; Xie, H.; Winterfeld, P. H.; Kneafsey, T. J.; Yin, X.; et al. CO<sub>2</sub> injection-induced fracturing in naturally fractured shale rocks. *Energy* **2017**, *139*, 1094–1110.
- (18) Yu, W.; Lashgari, H. R.; Wu, K.; et al. CO<sub>2</sub> injection for enhanced oil recovery in Bakken tight oil reservoirs. *Fuel* **2015**, *159*, 354–363.
- (19) Yan, H.; Zhang, J.; Li, B.; et al. Crack propagation patterns and factors controlling complex crack network formation in coal bodies during tri-axial supercritical carbon dioxide fracturing. *Fuel* **2021**, *286*, No. 119381.
- (20) Yang, X.; Wen, G.; Sun, H.; et al. Environmentally friendly techniques for high gas content thick coal seam stimulation-multi-discharge CO<sub>2</sub> fracturing system. *J. Nat. Gas Sci. Eng.* **2019**, *61*, 71–82.
- (21) Zhang, X.; Zhu, W.; Xu, Z.; Liu, S.; Wei, C. A review of experimental apparatus for supercritical CO<sub>2</sub> fracturing of shale. *J. Pet. Sci. Eng.* **2022**, *208*, No. 109515.
- (22) Wang, K.; Pan, H.; Zhang, T.; et al. Experimental study on the radial vibration characteristics of a coal briquette in each stage of its life cycle under the action of CO<sub>2</sub> gas explosion. *Fuel* **2022**, *320*, No. 123922.
- (23) Sampath, K.; Perera, M. S. A.; Ranjith, P. G.; et al. Qualitative and quantitative evaluation of the alteration of micro-fracture characteristics of supercritical CO<sub>2</sub>-interacted coal. *J. Supercrit. Fluids* **2019**, *147*, 90–101.
- (24) Xing, H. Z.; Wu, G.; Dehkoda, S.; et al. Fracture and mechanical characteristics of CO<sub>2</sub>-saturated sandstone at extreme loading conditions. *Int. J. Rock Mech. Min. Sci.* **2019**, *117*, 132–141.
- (25) Shang, Z.; Wang, H.; Li, B.; et al. Fracture processes in coal measures strata under liquid CO<sub>2</sub> phase transition blasting. *Eng. Fract. Mech.* **2021**, *254*, No. 107902.
- (26) Cai, C.; Kang, Y.; Yang, Y.; et al. The effect of shale bedding on supercritical CO<sub>2</sub> jet fracturing: A experimental study. *J. Pet. Sci. Eng.* **2020**, *195*, No. 107798.
- (27) Wang, K.; Pan, H.; Zhang, T. Experimental study of prefabricated crack propagation in coal briquettes under the action of a CO<sub>2</sub> gas explosion. *ACS Omega* **2021**, *6*, 24462–24472.
- (28) Huang, Y. H.; Yang, S. Q.; Hall, M. R. Fracture and strain field evolution in faulted brine-saturated sandstone. *J. Test. Eval.* **2018**, *48*, 1206–1225.
- (29) Orlhac, F.; Soussan, M.; Maisonobe, J. A.; et al. Tumor texture analysis in 18F-FDG PET: relationships between texture parameters, histogram indices, standardized uptake values, metabolic volumes, and total lesion glycolysis. *J. Nucl. Med.* **2014**, *55*, 414–422.
- (30) Hodgdon, T.; McInnes, M. D. F.; Schieda, N.; et al. Can quantitative CT texture analysis be used to differentiate fat-poor renal angiomyolipoma from renal cell carcinoma on unenhanced CT images? *Radiology* **2015**, *276*, 787–796.
- (31) Chen, S.; Li, F.; Yin, D.; et al. Experimental study on deformation failure characteristics of limestone–coal composite with different rock-coal height ratios. *J. Cent. South Univ.* **2023**, 1–14.
- (32) Xu, J.; Liu, F.; Chen, Z.; et al. Digital features of main constituents in granite during crack initiation and propagation. *Eng. Geol.* **2017**, *225*, 96–102.
- (33) Sun, C.; Cao, S.; Li, Y. Mesomechanics coal experiment and an elastic-brittle damage model based on texture features. *Int. J. Min. Sci. Technol.* **2018**, *28*, 639–647.
- (34) Zhang, K.; Zhang, K. Gray and texture features of strain field for fractured sandstone during failure process. *J. China Coal Soc.* **2021**, *46*, 1253–1262.
- (35) Yin, D.; Chen, S.; Ge, Y.; et al. Mechanical properties of rock-coal bi-material samples with different lithologies under uniaxial loading. *J. Mater. Res. Technol.* **2021**, *10*, 322–338.
- (36) Wang, G.; Wu, M.; Wang, R.; et al. Height of the mining-induced fractured zone above a coal face. *Eng. Geol.* **2017**, *216*, 140–152.
- (37) Wang, G.; Li, W.; Wang, P.; et al. Deformation and gas flow characteristics of coal-like materials under triaxial stress conditions. *Int. J. Rock Mech. Min. Sci.* **2017**, *91*, 72–80.

- (38) Wang, X.; Liu, X.; Wang, E.; et al. Experimental research of the AE responses and fracture evolution characteristics for sand-paraffin similar material. *Constr. Build. Mater.* **2017**, *132*, 446–456.
- (39) Zhai, C.; Xu, J.; Liu, S.; et al. Fracturing mechanism of coal-like rock specimens under the effect of non-explosive expansion. *Int. J. Rock Mech. Min. Sci.* **2018**, *103*, 145–154.
- (40) Singh, K.; Kapoor, R. Image enhancement via median-mean based sub-image-clipped histogram equalization. *Optik* **2014**, *125*, 4646–4651.
- (41) Chen, S.; Zhang, J.; Yin, D.; et al. Visualizing experimental investigation on gas-liquid replacements in a microcleat model using the reconstruction method. *Deep Underground Sci. Eng.* **2023**, 1–9.
- (42) Zhang, J.; Chen, S.; Ji, S.; et al. Imaging dynamic water invasion behavior in microfractures based on microfluidics. *J. Cent. South Univ.* **2022**, *29*, 3986–4001.
- (43) Farid, H.; Lyu, S. In *Higher-Order Wavelet Statistics and Their Application to Digital Forensics*, 2003 Conference on Computer Vision and Pattern Recognition Workshop; IEEE, 2003; pp 94.
- (44) Vincent, L. Morphological grayscale reconstruction in image analysis: applications and efficient algorithms. *IEEE Trans. Process.* **1993**, *2*, 176–201.
- (45) Bhandarkar, S. M.; Luo, X.; Daniels, R.; et al. Detection of cracks in computer tomography images of logs. *Pattern Recognit. Lett.* **2005**, *26*, 2282–2294.
- (46) Kondrat'ev, V. A. F. M. Arscott, Periodic differential equations. *Usp. Mat. Nauk* **1967**, *22*, 272–273.
- (47) Liu, S.; Yang, Y.; Cao, Y.; et al. A summary on the research of GRA models. *Grey Syst. Theory Appl.* **2013**, *3*, 7–15.
- (48) Taylor, J. R.; Thompson, W. *An Introduction to Error Analysis: The Study of Uncertainties in Physical Measurements*; University Science Books: Mill Valley, CA, 1982.
- (49) Chen, S.; Ge, Y.; Yin, D.; et al. An experimental study of the uniaxial failure behaviour of rock-coal composite samples with pre-existing cracks in the coal. *Adv. Civ. Eng.* **2019**, *2019*, No. 8397598.
- (50) Nilson, R. H.; Proffer, W. J.; Duff, R. E. Modelling of gas-driven fractures induced by propellant combustion within a borehole. *Int. J. Rock Mech. Min. Sci. Geomech. Abstracts* **1985**, *22*, 3–19.
- (51) Haralick, R. M.; Shanmugam, K.; Dinstein, I. H. Textural features for image classification. *IEEE Trans. Syst. Man, Cybernetics* **1973**, *6*, 610–621.
- (52) Wang, K.; Pan, H.; Fujii, Y. Study on energy distribution and attenuation of CO<sub>2</sub> fracturing vibration from coal-like material in a new test platform. *Fuel* **2024**, *356*, 129584.